International Journal of Fatigue 215 (2027) 109952

Contents lists available at ScienceDirect

International Journal of Fatigue

journal homepage: www.elsevier.com/locate/ijfatigue

Neural network-based framework for fatigue life prediction of natural rubber under thermo-oxidative preaging spectra

Ala Hijazi [a,b,*], Sameer Al-Dahidi [a,c]

[a] Department of Mechanical and Maintenance Engineering, German Jordanian University, Amman, Jordan
[b] Department of Aeronautical Engineering, Istanbul Gelisim University, Istanbul, Turkey
[c] Industrial and Systems Engineering Department, King Fahd University of Petroleum and Minerals, Dhahran, Saudi Arabia

ARTICLE INFO

Keywords:
ANN
PINN
Optimization
Natural rubber
Thermo-oxidative aging
Spectral aging
Fatigue life
Incremental-degradation
Machine learning

ABSTRACT

Thermo-oxidative (TO) preaging significantly influences the fatigue behavior of natural rubber (NR). However, existing artificial neural network (ANN) models are generally limited to isothermal aging conditions and cannot directly represent multi-temperature preaging spectra encountered in practical applications. This study develops a framework for extending ANN-based fatigue-life predictors trained exclusively using isothermal preaging data to multi-temperature aging histories. An optimized physics-informed neural network (PINN) is employed as the underlying fatigue-life predictor, incorporating a physics-based constraint to preserve the expected power-law behavior of the generated S-N curves. Two spectral-aging representations are investigated. The first converts the aging spectrum into an equivalent isothermal condition using weighted-mean-temperature or Arrhenius-based equivalent-time formulations. The second introduces an incremental-degradation representation in which the individual aging steps are evaluated sequentially while accounting for the preceding aging history. The optimized PINN achieves mean absolute percentage errors (MAPE) of 16.5% and 14.8% for unseen data within the training conditions and left-out isothermal aging conditions, respectively. For spectral preaging, the Arrhenius-based equivalent-time method substantially outperforms the weighted-mean-temperature approach. The proposed incremental-degradation representation provides the highest accuracy, with a MAPE of 6.13%, while preserving the sequential nature of the aging process and avoiding the need for a global reference temperature. Its predictions are also in close agreement with the experimental S-N curve and compare favorably with the analytical Neuhaus model, without requiring explicit determination of temperature and displacement dependent activation-energy parameters. The proposed methodology therefore provides a practical approach for extending isothermally trained ANN-based fatigue-life models to multi-temperature preaging histories.

1. Introduction

Elastomers are types of polymers known for their high deformability, resilience, and ability to recover large strains upon unloading. Among them, natural rubber (NR) is one of the most widely used materials due to its outstanding flexibility, toughness, crack-growth resistance, and vibration isolation capability. These properties make NR essential in industrial, construction, automotive, aerospace, and medical applications. In particular, black-filled NR is widely used in tires, engine mounts, vibration isolators, seals, tubes, and cable insulation systems. In such applications, components are routinely subjected to cyclic loading. Consequently, reliable fatigue life prediction of NR components is of primary importance for ensuring structural integrity, durability and service reliability.

Fatigue behavior of NR is commonly characterized through load-life (S-N) relationships derived from cyclic testing. Extensive investigations have examined the damage mechanisms and fatigue life in NR [1–5]. However, in real service conditions, elastomeric components are rarely exposed to mechanical loading alone. Instead, they operate in complex thermo-mechanical environments involving elevated temperatures, oxygen diffusion, and long-term exposure to oxidative conditions. Elevated temperature can induce both reversible viscoelastic effects and irreversible microstructural changes in NR [6]. Temperature rise may result from external heat sources (e.g., combustion engines) or internal self-heating due to hysteretic energy dissipation under dynamic loading [7–9], a phenomenon particularly critical in vibration isolation

* Corresponding author at: Department of Mechanical and Maintenance Engineering, German Jordanian University, Amman, Jordan.
E-mail address: Ala.Hijazi@gju.edu.jo (A. Hijazi).

https://doi.org/10.1016/j.ijfatigue.2026.109952
Received 30 June 2026; Received in revised form 16 August 2026; Accepted 24 August 2026
Available online 29 August 2026
0142-1123/

applications.

Experimental investigations indicate that the fatigue life of NR decreases with increasing temperature, where there is often a threshold temperature beyond which degradation accelerates [10]. Ruellan et al. [11] demonstrated that both crack initiation and crack growth in NR are strongly temperature-dependent, with thermo-mechanical coupling and strain-induced crystallization significantly influencing fatigue resistance. When NR is exposed to elevated temperatures for extended periods prior to mechanical loading, thermo-oxidative (TO) aging occurs. This process involves oxidation-driven chain scission and/or additional crosslinking reactions, leading to changes in crosslink density, stiffness, and fracture properties [5,12]. The competition between chain scission and crosslinking alters the network structure and, consequently, the fatigue resistance of the material [13]. Abdelaziz et al. [14] investigated fracture behavior of aged rubbers and emphasized the importance of predictive tools capable of accounting for aging-induced property changes. Neuhaus et al. [6] systematically examined the coupled influence of TO preaging and testing temperature on NR fatigue life. In that study, they introduced a reasonably accurate semi-empirical analytical framework capable of predicting fatigue life under combined aging and temperature effects.

In practical service conditions, rubber components are often subjected to preaging spectra, where components experience multiple temperature levels over different durations during their life cycle. Such non-isothermal or multi-step aging histories cannot be fully described by single-temperature aging parameters. From a physico-chemical standpoint, oxidation kinetics in elastomers are strongly temperature-dependent and frequently modeled using Arrhenius-type formulations [15,16]. For variable-temperature histories, the cumulative aging effect may be represented through time–temperature superposition or equivalent aging time concepts, where the temperature-dependent reaction rate is integrated over exposure time [17]. However, translating such cumulative degradation measures into reliable fatigue life predictions remains challenging, particularly when fatigue mechanisms themselves are temperature sensitive.

Traditional analytical fatigue models typically rely on fitted S-N relationships, fracture mechanics approaches, or damage evolution laws calibrated for specific environmental conditions [17]. While these models are effective under controlled conditions, they often struggle to generalize across different aging temperatures and durations. This limitation arises from the complex interaction between thermal aging kinetics and fatigue behavior. Consequently, capturing these coupled effects within a closed-form analytical framework becomes even more challenging when the preaging history is non-isothermal.

Artificial Neural Networks (ANNs), offer a data-driven approach capable of approximating highly nonlinear relations between inputs and outputs [18]. In recent years, ANNs have been successfully applied to fatigue life prediction across various materials [19–23], including NR. Also, several studies utilized ANNs for evaluating the effects of temperature on the properties and fatigue behavior of NR. Liu et al. [24] developed a back-propagation ANN optimized via an improved sine–cosine algorithm to predict NR fatigue life using peak engineering strain, ambient temperature, and Shore hardness as inputs, achieving high predictive accuracy. Robin et al. [25] demonstrated that scholastically structured data repetition strategies can enable reliable fatigue prediction across temperatures even with limited datasets. Hybrid approaches integrating physical constraints have further improved robustness of ANN-based approaches. Sun et al. [26] incorporated physical fatigue-life estimates within a Physics-Informed Neural Network (PINN) framework, enhancing predictive consistency. Liu et al. [27] explicitly addressed testing temperature effects using PINN, achieving predictions with good accuracy at temperatures up to 110°C. Li et al. [28] extended the PINN framework to characterize TO aging effects in viscoelastic materials by embedding microsphere-based physical constraints. Furthermore, Hijazi et al. [29] used ANN-based modeling for evaluating the fatigue life of NR under combined TO preaging and testing temperature effects. Several ANN modeling approaches, including purely data-driven ANN, Assisted-ANN, and PINN, were employed to predict S-N relationships across different preaging temperatures, aging durations, and testing temperatures. Their results demonstrate the superior predictive performance of ANN-based models, particularly the PINN approach, as compared with the semi-empirical analytical formulation proposed in [6], with evaluation based on both statistical error metrics and physical consistency of the predicted S-N curves.

The previously mentioned ANN-based models for fatigue life prediction of NR have primarily addressed either testing temperature effects, TO preaging effects, or the combination of the two. Despite these advances, the generalization of fatigue life prediction under multi-step preaging spectra remains unexplored. In particular, it is unclear how ANN-based models can effectively handle cumulative TO history and extrapolate fatigue life beyond single-temperature (isothermal) aging conditions.

The present study addresses this gap by employing comprehensive experimental dataset [6,29], comprising S-N data under different isothermal preaging conditions covering temperatures up to 120°C, and aging durations up to 2088 h. Unlike previous investigations that dealt with preaging as a single isothermal condition, this work extends the applicability of ANN-based modeling toward representing and predicting the fatigue life of NR under preaging spectra, where aging is conducted at different temperatures for different durations prior to testing. The PINN modeling approach is adopted in this study as it has previously been shown to generate more physically consistent S-N curves than other ANN-based approaches [29]. A rigorous multi-objective optimization procedure is carried out to determine the PINN architecture and training parameters that provide the best balance between prediction accuracy and physical consistency. The PINN is trained using fatigue data obtained under isothermal preaging conditions and is subsequently used to predict fatigue life under multi-temperature preaging conditions. Different approaches are proposed for representing multi-step preaging spectra using the isothermally trained PINN, and their predictive performance is evaluated against experimental results. In addition, a novel incremental-degradation representation is introduced, in which the PINN is applied sequentially to the individual steps of the aging spectrum and the cumulative degradation is determined while accounting for the preceding aging history. The principal contribution of this study is not the development of a new PINN architecture, but the formulation and evaluation of spectral-aging representations that enable an ANN-based fatigue-life predictor trained exclusively using isothermal preaging data to handle multi-temperature aging histories.

By integrating cumulative TO aging representation with PINN modeling, this study aims to provide a robust framework for predicting the fatigue life of NR, and polymers in general, under realistic service-like aging histories. Although the present study focuses on TO preaging spectra, the proposed ANN-based framework is fundamentally methodology-driven rather than condition-specific. Therefore, this framework can potentially be extended to other complex service scenarios such as variable-amplitude fatigue loading and multi-physics environmental degradation conditions.

The remainder of this paper is organized as follows. Section 2 summarizes the analytical fatigue-life framework, ANN modeling principles, and the PINN approach adopted in this study. Section 3 describes the experimental dataset, while Sections 4 and 5 present the ANN dataset design and the PINN modeling procedure, respectively. Section 6 introduces the proposed methodologies for extending the PINN framework to thermo-oxidative preaging spectra. Section 7 presents and discusses the optimization results and the predictive performance of the proposed approaches. Finally, Section 8 summarizes the main conclusions.

2. Theory

2.1. Analytical fatigue life prediction

An analytical (semi-empirical) framework for predicting the fatigue life of NR as a function of displacement level, thermal preaging, and test temperature effects was proposed by Neuhaus et al. [6,30]. This analytical framework was later employed by Hijazi et al. [29], where its predictive accuracy was compared with that of ANN-based approaches. The framework utilizes an experimentally fitted power-law baseline S-N relationship and applies modifications to account for the effects of preaging and test temperature. Since the fatigue experiments considered in the present work are conducted at room temperature and relatively low frequency (4 Hz) to minimize self-heating effects, only the influence of preaging is considered here.

First, the reference “unaged” fatigue life of the material as a function of displacement amplitude d is described using a power-law relation as:

$$N_0(d) = K\,d^{\,b} \tag{1}$$

where N_0 is the number of cycles to failure, d is the imposed displacement amplitude, and K and b are material constants obtained by fitting Eq. (1) to the experimental data. For unaged NR specimens (with material composition as stated in Section 3), the material constants are found to be $K = 8.139 \times 10^8$ and $b = -3.279$ [29].

The reduction of fatigue life resulting from preaging at temperature T_a for a duration t_a is then accounted for using an exponential decay law as:

$$N_a(T_a, t_a, d) = N_0(d)\exp - \left(\frac{t_a}{\tau_s(T_a, d)}\right) \tag{2}$$

where N_a is the fatigue life after preaging and $\tau_s(T_a, d)$ is the characteristic aging time, defined as the aging duration required for the fatigue life to decrease to $1/e$ of its initial value. The value of the characteristic aging time τ_s depends on both ageing temperature T_a and displacement d. For each aging temperature, the corresponding τ_s value is obtained by fitting Eq. (2) to the experimental fatigue life at a constant displacement level. The characteristic time can also be represented using the Arrhenius relation as:

$$\tau_s(T_a, d) = \left[\nu(T_a, d)\exp\left(-\frac{E_a(T_a, d)}{RT_a}\right)\right]^{-1} \tag{3}$$

where ν is the pre-exponential factor, E_a is the activation energy, R is the universal gas constant. Based on their experimental results, Neuhaus et al. [6] reported that the activation-energy (E_a) values for NR depend on both the preaging-temperature range and the load level (displacement). The empirically determined characteristic ageing times for NR at different aging temperatures and displacement levels are reported in [6]. The accuracy of the analytical model predictions is strongly dependent on the accuracy of the characteristic aging times used in the calculations. Previous investigations by the authors [29] have shown that ANN-based approaches provide superior predictive accuracy compared with this analytical framework.

For a multi-step preaging spectrum, the Neuhaus et al. [6] formulation can be extended by accumulating the contribution of the individual temperature-duration segments. Accordingly, the fatigue life after a spectrum consisting of n aging steps can be expressed as:

$$N_{\text{spec}}(d) = N_0(d)\exp\left[-\sum_{i=1}^{n}\frac{t_i}{\tau_s(T_i, d)}\right] \tag{4}$$

where T_i and t_i denote the temperature and duration of the i-th aging step, respectively, and $\tau_s(T_i, d)$ is the corresponding displacement-dependent characteristic aging time. This analytical formulation was previously applied to the same four-step preaging spectrum considered in the present work. Accordingly, the analytical model is used in the present study as a reference benchmark for comparison with the proposed ANN-based spectral-aging prediction approaches.

2.2. ANN modeling

ANNs are data-driven models capable of approximating complex nonlinear relationships between input and output variables [18]. The available data are generally divided into training, validation, and testing subsets. The training set is used to optimize the network parameters, the validation set is employed to monitor the learning process and reduce overfitting, and the testing set is reserved for evaluating the predictive performance of the trained model on unseen data. During training, network weights and biases are iteratively adjusted to minimize the difference between predicted and target responses. ANN models do not require an explicit closed-form representation of the underlying physical processes. As a result, ANNs have become a widely used alternative to complex analytical formulations and computationally demanding numerical models. Their primary advantage lies in their ability to accurately capture complex nonlinear relationships involving multiple input and output variables without requiring prior knowledge about the governing physical mechanisms.

2.3. Physics-based ANN modeling

Conventional ANNs are purely data-driven and do not inherently enforce known physical behavior. To improve prediction robustness, especially for small or sparse datasets, physics-based machine learning approaches have been developed that combine data-driven learning with physical or analytical knowledge [31–37]. Among these approaches, Assisted-ANN and Physics-Informed Neural Networks (PINNs) represent two distinct strategies.

In Assisted-ANN approaches, such knowledge is introduced through additional input parameters derived from analytical or semi-empirical models [29,33]. Hijazi et al. [33] demonstrated that Assisted-ANN models can significantly improve prediction accuracy and robustness compared to conventional ANNs, particularly when limited datasets are available. Due to their simplicity and flexibility, Assisted-ANN approaches are especially attractive when governing equations are incomplete or difficult to enforce.

In contrast to the Assisted-ANN approach, PINNs directly embed governing equations, constitutive relations, and boundary or initial conditions into the ANN loss function, forcing the network to satisfy physical constraints during training. This approach can improve robustness and physical consistency, particularly when experimental datasets are relatively small or sparse. Since their introduction by Raissi et al. [32], PINNs have been widely applied in solid mechanics, fluid dynamics, and materials modeling [29,34–37].

Previous work by Hijazi et al. [29] compared purely data-driven traditional ANN with Assisted-ANN and PINN approaches for predicting the fatigue life of NR under combined effects of TO preaging and test temperature effects. Their results demonstrated that PINNs provide superior prediction accuracy and robustness when the training dataset is small and sparse. The study also showed that PINN predictions are more consistent with the known physics governing the S-N relationship, highlighting the capability of PINNs to produce physically meaningful fatigue-life predictions while maintaining strong predictive performance. For this reason, the PINN approach is adopted in the current work, particularly because the ANN must closely preserve the physics governing the load-life relationship in order to reliably handle the spectral preaging conditions.

3. Experimental data

The fatigue experiments were conducted on a carbon black-filled NR blend typically used in general industrial applications. The material consists of 90% NR and 10% polybutadiene, with a Shore A hardness of 48 [6]. Vulcanization was achieved using a sulfur-based cross-linking system, and appropriate antioxidants and antiozonants were incorporated to mitigate premature ageing.

Uniaxial fatigue tests were performed on hourglass-shaped specimens under load-control conditions with fully reversed loading (stress ratio $R = -1$). All tests were carried out at room temperature at a test frequency of 4 Hz (to minimize dissipative self-heating effects). The displacement corresponding to the tensile portion of the cyclic response (specifically, the steady-state displacement after the first 1000 cycles) was used in constructing the S-N diagrams. The tensile displacement, rather than applied force or stress, is commonly used as the fatigue damage parameter in studies involving preaged elastomers, since it simplifies the analytical modeling of fatigue behavior [6]. To adequately capture the relationship between load (i.e., tensile displacement) and fatigue life, tests were conducted at three load levels (namely; 120 N, 150 N, and 180 N) for each of the different preaging conditions. Additionally, multiple replicates (generally three to four per load level) were tested to improve statistical reliability. Further details about the experimental procedures can be found in [30].

Based on their preaging history, the specimens considered in this investigation are classified into three categories: (i) unaged, (ii) isothermally preaged at a fixed temperature for a specified duration, and (iii) preaged under multi-temperature spectrum (spectral preaging). The unaged specimens serve as the reference condition for establishing the baseline S-N relationship of the material. For isothermal preaging, four temperatures (70 °C, 85 °C, 100 °C, and 120 °C) are used in the experiments, with aging durations ranging from 16 to 2088 h. In total, 18 distinct isothermal preaging conditions are considered in this investigation, as summarized in Table 1. For the spectral preaging condition, specimens are sequentially exposed to four different temperatures prior to fatigue testing, as detailed in Table 2. In total, the complete experimental test matrix considered in this study includes 237 data points. Owing to its size, the complete dataset is not included in this paper.

The experimentally obtained S-N diagram for specimens subjected to spectral preaging, along with the corresponding power-law fit is shown in Fig. 1. The figure shows noticeable variations in tensile displacement for the duplicates tested at identical force levels (similar variations are also seen for all the other preaging conditions). To further illustrate the variations observed in the figure, duplicate tests at each load level are grouped within red rectangles in the figure. This variability in displacement is primarily attributed to inherent differences in specimen stiffness. Furthermore, a significant scatter in fatigue life is also observed among duplicates, which is consistent with the inherently stochastic nature of the fatigue phenomena. For the dataset considered in this study, the average lifetime dispersion of the duplicates (defined as the absolute deviation from the mean) is approximately 18.1×10^3 cycles.

Table 1
The different isothermal preaging conditions used in the experiments (* conditions not used for network training).

Cond. No.	Preaging Temp. (°C)	Preaging Duration (hour)	Cond. No.	Preaging Temp. (°C)	Preaging Duration (hour)
1	70	180	10	100	25
2	70	550	11	100	82
3	70	1000	12	100	264
4	70	2088	13	100	504
5	85	36	14	120	16
6	85	117	15	120	24
7	85	384	16	120	48
8	85	858	17*	85	180
9	85	1200	18*	100	120

Table 2
The preaging spectrum used in the experiments (steps performed in sequence).

Step ID	Preaging Temp. (°C)	Preaging Duration (hour)
A	70	287.4
B	85	127.3
C	100	24.5
D	120	7.6

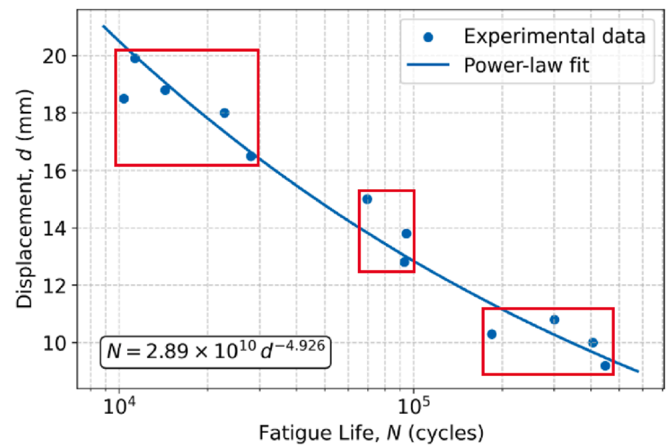

Fig. 1. Experimental S-N diagram along with fitted power-law curve for specimens subjected to spectral preaging (Table 2). Points inside rectangular shapes are duplicates tested at same force.

4. ANN datasets design

For ANN modeling, the experimental dataset is typically divided into training, validation, and testing subsets, where the datapoints assigned to each are randomly selected. The typical distribution of datapoints among these subsets ranges between (60%, 20%, 20%) and (70%, 15%, 15%) for the training, validation, and testing datasets, respectively. However, for the dataset at hand, a random split of the available data is not the most appropriate approach, given that multiple duplicates are available for each testing condition and fatigue load level. In addition, it is desirable to train the network using conditions where preaging is performed at fixed temperatures and durations, and then to evaluate the network's generalization capability by predicting fatigue life under spectral preaging conditions.

Accordingly, the training and validation datasets are randomly selected from the duplicate measurements of the: i) unaged specimens and ii) specimens with isothermal preaging corresponding to conditions (1) to (16) (listed in Table 1). It should be noted that preaging conditions (17) and (18) are not used for training, and they will only be included in the testing dataset. Accordingly, the training and validation datasets consist of 110 and 34 datapoints (i.e., 47% and 15% of the total available datapoints), respectively. It should be noted that, although several duplicate tests are performed at each force level, these duplicates can be treated as independent measurements from an ANNs modeling perspective, since displacement is reported rather than the force (given the high variability in displacement observed in Fig. 1).

For the unaged (virgin) material condition, instead of developing a conditional network to handle unaged and aged conditions separately, corresponding values of aging temperature and aging duration are assigned during ANN training. Specifically, the aging temperature is set to 25°C and the aging duration is set to zero hours. However, the ANN does not inherently recognize that a zero aging duration corresponds to the unaged condition regardless of the specified temperature. To overcome this issue, the datapoints of the unaged condition are replicated and assigned to additional input combinations corresponding to 70°C, 85°C, 100°C, and 120°C, each with an aging duration of zero hours. Consequently, 44 additional datapoints corresponding to four extra (unaged) conditions are added to the training and validation datasets, increasing the total number of training and validation datapoints to 188. It is worth mentioning here that it is also possible to overcome the issue of zero aging duration and enforce the condition $N(T, 0, d) = N_0(d)$ by mathematically embedding a physical boundary condition directly into the PINN architecture. However, such approach was found to reduce the prediction accuracy at short aging durations.

The dataset used for testing the predictive performance of the ANN is divided into three subgroups representing progressive levels of evaluation. The first testing subgroup corresponds to the initial level of testing and consists of the remaining datapoints for the unaged condition and isothermal preaging conditions (1) to (16) (i.e., the datapoints that are not included in the training and validation datasets). This subgroup contains 51 datapoints (i.e., 22% of the complete dataset). The second testing subgroup represents a higher level of evaluation and includes datapoints of the two left-out conditions (LOC)s that are not used during training (i.e., preaging conditions (17) and (18), as indicated in Table 1). This subgroup comprises 20 datapoints (i.e., 9% of the complete dataset), with 10 datapoints for each condition. The third testing subgroup represents the highest level of evaluation and consists of datapoints corresponding to the spectral preaging condition (Table 2). This subgroup contains 12 datapoints (i.e., 5% of the complete dataset), which were previously shown in Fig. 1. Combining the three subgroups shows that the testing dataset is relatively large, comprising 36% of the complete experimental dataset, where this enhances confidence in evaluating the ANN's predictive performance on unseen data. It should also be emphasized that the training and validation datasets include only datapoints corresponding to unaged and isothermally preaged conditions, with no data points associated with spectral preaging conditions.

The adopted structure of the testing dataset provides a hierarchical framework for evaluating the predictive capability of the ANN. It provides a progressive assessment of model generalization, ranging from unseen datapoints under known isothermal conditions to unseen isothermal aging conditions and, finally, spectral preaging conditions.

5. PINN modeling procedure

5.1. Network architecture

The PINN approach adopted in this study employs a dual neural-network architecture consisting of a main data-driven "regression" network and an auxiliary physics-based network. The data-driven network is responsible for predicting fatigue life directly from the experimental input variables, whereas the auxiliary physics network is introduced to enforce physical consistency during training through a physics-based loss formulation. The data-driven network architecture consists of an input layer defining the fatigue test conditions, a single hidden layer, and an output layer with one neuron representing fatigue life. The input layer includes three variables: preaging temperature (T_a), preaging duration (t_a), and tensile displacement (d). Fig. 2 presents a schematic illustration of the adopted PINN architecture.

Instead of using the raw fatigue-life values as the output target, the fatigue life (N) is transformed into logarithmic space, $\log_{10}(N)$, and used as the network output variable. In practice, modeling fatigue life in logarithmic space improves the statistical properties of the dataset used for model development and reduces the influence of extreme values, leading to more robust regression behavior. This transformation is particularly beneficial for small and highly scattered fatigue datasets [29]. Accordingly, the network directly predicts $\log_{10}(\widehat{N})$, from which the actual fatigue life is subsequently determined.

Pearson correlation analysis is performed using the training and validation datasets to investigate the influence of the input variables on

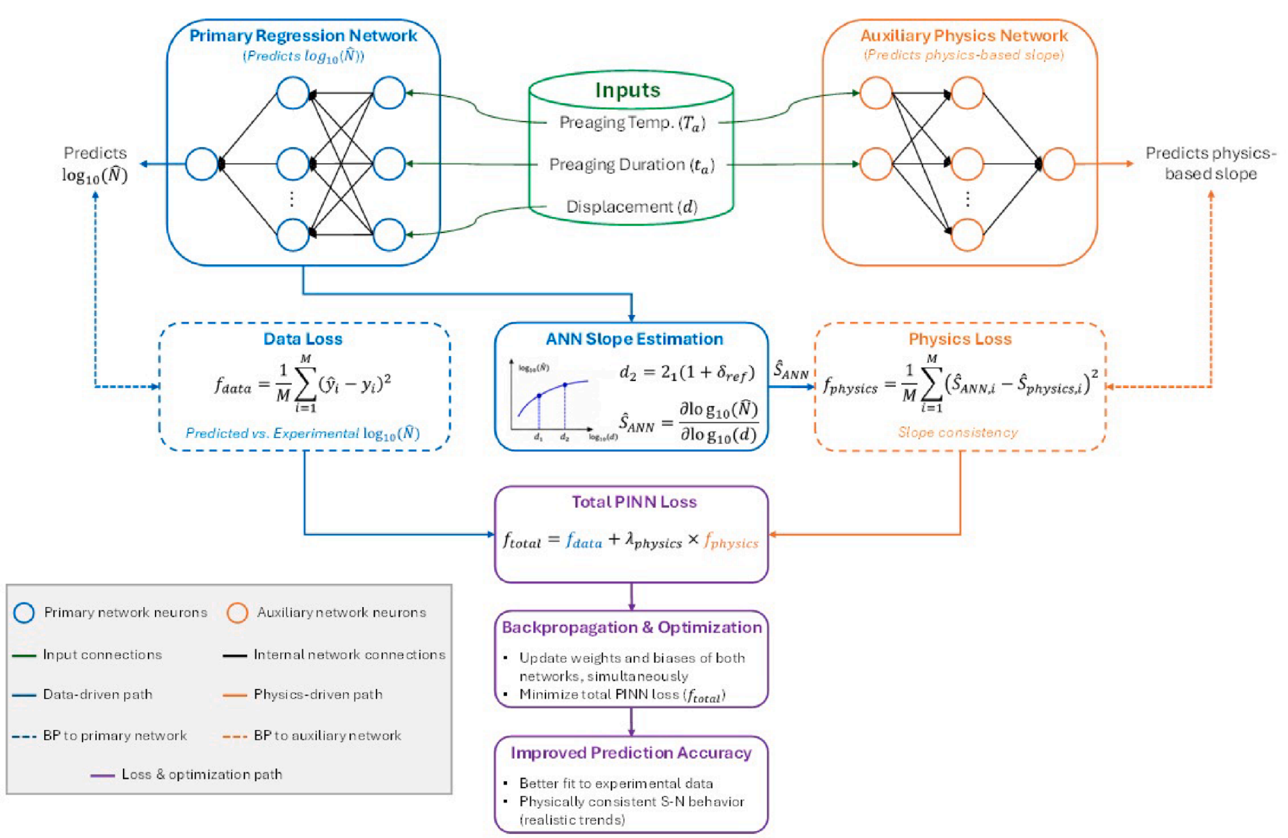

Fig. 2. Schematic illustration of the proposed PINN approach architecture.

the target variable (fatigue life). The correlation results show that displacement (d) has the strongest relationship with fatigue life (N) (i.e., -0.65), followed by preaging duration (t_a) (i.e., -0.3), while preaging temperature (T_a) exhibits the weakest correlation (i.e., -0.04). These results indicate that the fatigue behavior of the material is governed primarily by the applied displacement (i.e., load level). Therefore, the assessment of the PINN models in this study focuses not only on prediction error metrics, which are evaluated at a limited number of data points, but also on the physical consistency of the generated S-N curves. Furthermore, the physics-based component of the PINN focuses on preserving the established load-life relationship, while the more complex effects of preaging temperature and duration are learned from the experimental data, as further discussed in Section 5.2.2.

Because the number of input and output variables is limited, a single hidden layer is adopted. Previous investigations have demonstrated that shallow networks provide good predictive capability for comparably small datasets [29,33,38,39]. Rather than selecting the number of hidden neurons using an empirical rule [24,27,40,41], the network size is determined through the optimization procedure described in Section 5.3.

5.2. Modeling approach

The proposed PINN approach incorporates prior fatigue-behavior knowledge directly into the traditional training process through a combined data-driven and physics-guided learning strategy. In addition to minimizing the difference between the experimentally (N) and predicted ($\widehat{N}$) observed fatigue-life values, the proposed PINN approach introduces an additional physics-based constraint to ensure that the generated fatigue S-N curves remain physically realistic.

The detailed modeling aspects of developed PINN framework are presented in the following subsections. Section 5.2.1 describes the implementation of the primary regression network, whereas Section 5.2.2 presents the auxiliary physics network and the adopted physics-enforcement strategy.

5.2.1. Primary regression network

The primary regression network predicts logarithmic fatigue life from preaging temperature, preaging duration, and tensile displacement. The input variables are normalized using the mean and standard deviation of the training dataset to improve numerical stability. The number of hidden neurons and activation function are determined through the optimization procedure described in Section 5.3, while the single output neuron provides the predicted logarithmic fatigue life, which is subsequently transformed back to the original fatigue-life scale.

The data-driven loss of the primary network (f_{data}) represents the traditional data-driven loss term and is defined as the Mean Square Error (MSE) between each i-th actual/experimental value and predicted logarithmic fatigue life value (Eq. (5)), where $i = 1, \cdots, M$, and M denotes the total number of training samples:

$$f_{data} = \frac{\sum_{i=1}^{M} (\widehat{y}_i - y_i)^2}{M} \tag{5}$$

The primary network is trained within the custom PINN training loop together with the auxiliary physics network. The network parameters are updated using a gradient-based optimization algorithm, as will be explained in Section 5.3.

5.2.2. Auxiliary physics network

The auxiliary physics network is incorporated into the proposed PINN approach to enforce physical consistency during the training process. Unlike the primary regression network, which directly predicts fatigue life, the auxiliary network is responsible for learning the physics-based slope behavior associated with the typical power-law S-N relationship (Eq. (1)), describing the dependence of fatigue life (N) on tensile displacement (d). In logarithmic form, the relationship can be written as:

$$\log_{10}(N) = \log_{10}(K) + b \times \log_{10}(d) \tag{6}$$

where K is a condition-dependent material constant and b represents the fatigue life slope parameter. This formulation indicates that fatigue life varies linearly with displacement in log–log space. Instead of directly imposing the complete analytical power-law equation explicitly during training, the proposed PINN approach constrains the local logarithmic slope of the generated S-N curves. Accordingly, the governing physical behavior is introduced through the following slope expression:

$$b = \frac{\partial \log_{10}(N)}{\partial \log_{10}(d)} \tag{7}$$

The physics-based constraint adopted in the present PINN is intentionally limited to the well-established power-law relationship between displacement and fatigue life. Among the considered inputs, displacement exhibits the strongest correlation with fatigue life and governs the physical shape of the predicted S-N curves. In contrast, the effects of preaging temperature and duration are learned directly from the experimental data rather than prescribed through an additional thermo-oxidative kinetic constraint. Introducing such a constraint would increase the complexity of the model and could impose an overly restrictive monotonic degradation behavior. In particular, the experimental results show that short preaging durations can improve fatigue life at low displacement levels before degradation becomes dominant at longer durations. Retaining a data-driven representation of the aging variables therefore allows the network to capture this nonmonotonic behavior while the physics-based loss preserves the established load-life relationship.

The auxiliary physics network consists of three layers: an input layer, a hidden layer, and an output layer. Specifically:

- The input layer consists of two neurons/nodes corresponding to the preaging temperature (T_a) and preaging duration (t_a).
- The hidden layer consists of 10 neurons and employs a tanh activation function. This simple fixed architecture is adopted because the auxiliary network has the specific role of learning the condition-dependent S-N slope behavior, as further discussed in Section 5.3.
- The output layer consists of one neuron/node corresponding to the predicted physics-based fatigue slope ($\widehat{S}_{physics}$).

The outputs of the two networks are then coupled through a combined loss function consisting of a data-driven loss component (f_{data}) and a physics-based loss component ($f_{physics}$), as follows:

$$f_{total} = f_{data} + \lambda_{physics} f_{physics} \tag{8}$$

The physics-based loss term of the auxiliary network ($f_{physics}$) is introduced to minimize the mismatch between the local slope estimated from the primary-network predictions and the corresponding slope predicted by the auxiliary physics network. The physics-loss term is formulated as:

$$f_{physics} = \frac{\sum_{i=1}^{M} \left(\widehat{S}_{ANN_i} - \widehat{S}_{physics_i}\right)^2}{M} \tag{9}$$

where $\widehat{S}_{ANN_i}$ denotes the i-th local logarithmic slope estimated from the main network predictions, while $\widehat{S}_{physics_i}$ represents the corresponding i-th condition-dependent slope predicted by the auxiliary physics network, $i = 1, \cdots, M$. The relative contribution of the physics-based loss term is controlled using the weighting coefficient ($\lambda_{physics}$), which is progressively increased during training in order to improve optimization stability and prevent excessive early-stage physics enforcement. It should be emphasized that the physics loss acts as a slope-based regularization term rather than independently guaranteeing the true material behavior. The primary network remains anchored to the experimental fatigue-life data through the supervised data loss, while slope consistency is promoted through the auxiliary network. Physical consistency is further considered during model selection through the PD criterion alongside MAPE, as will be described later in Section 5.3.

To estimate the ANN-generated local slope numerically ($\widehat{S}_{ANN}$), a small perturbation was applied to the displacement input. For each displacement value d_1, a neighboring displacement point $d_2 = d_1(1+\delta_{rel})$ was generated, where $\delta_{rel} = 0.01$. The corresponding ANN predictions were then used to compute the local slope through a finite difference approximation in logarithmic space. This slope estimate was subsequently incorporated into the physics-based loss function ($f_{physics}$).

5.3. PINN performance optimization

A comprehensive optimization procedure is employed to identify the optimal PINN configuration that provides both accurate fatigue life prediction and physically consistent S-N behavior. The optimization process is performed using only the training and validation datasets, while the independent unseen testing datasets are reserved exclusively for the final evaluation of the optimized model.

The optimization study investigates the influence of the following parameters within the primary regression network:

- The number of hidden neurons (H). The number of hidden neurons is assumed to vary from 1 to 20, covering both relatively small and relatively large network structures.
- The network's activation function (f). Four activation functions are investigated, namely Sigmoid, Hyperbolic Tangent (tanh), Rectified Linear Unit (ReLU), and Leaky ReLU [42].
- The network's optimization algorithm (l). Three gradient-based optimization algorithms are investigated during the training process, namely Adaptive Moment Estimation (Adam), Stochastic Gradient Descent with Momentum (SGDM), and Root Mean Square Propagation (RMSProp).

Thus, the total number of PINN configurations investigated will be $20 \times 4 \times 3 = 240$ different configurations. For each configuration, the PINN model is trained using a maximum of 5000 epochs with a learning rate of 10^{-3} and a mini-batch size of 256 samples. In addition, the physics-based weighting parameter ($\lambda_{physics}$) is progressively increased during training up to a maximum of 0.02 in order to improve convergence stability and avoid excessive early-stage physics-enforcement. Within the auxiliary physics network, the number of hidden neurons remains fixed at 10 neurons and the *tanh* activation function is employed. It is worth mentioning that the optimization is applied only to the primary regression network, since this network is responsible for learning the complex nonlinear relationship between the experimental inputs and fatigue life. In contrast, the auxiliary physics network has a more specific, lower-dimensional role of learning the expected S-N slope behavior as a function of the preaging conditions and providing physics-based regularization during training. Therefore, a simple fixed architecture consisting of one hidden layer with 10 neurons and a tanh activation function is adopted for the auxiliary network. Keeping this architecture fixed also limits the dimensionality and computational cost of the hyperparameter search, while the multi-objective optimization focuses on balancing prediction accuracy (MAPE) and physical consistency (PD).

The predictive capability of each PINN configuration is evaluated using two performance metrics computed based on the combined training and validation datasets. The first performance metric quantifies the numerical accuracy of the predictions, whereas the second metric evaluates the physical consistency of the generated S-N curves. Unlike conventional error metrics, the second metric is intended for qualitative assessment of the predicted fatigue-life relationships. It provides a numerical measure of the extent to which the shape of the generated S-N curves conforms to the expected physics-based power-law behavior. Accordingly, the optimization problem is formulated as a multi-objective optimization problem that considers both the prediction accuracy and physical consistency when selecting the optimal PINN configuration.

- Mean Absolute Percentage Error (MAPE). It is used to quantify the capability of the model to provide accurate prediction results. Specifically, it evaluates the average percentage deviation between the actual/experimental and predicted fatigue life values, as shown in Eq. (10). Smaller MAPE values indicate superior predictive capability of the adopted PINN configuration, and vice-versa:

$$\mathrm{MAPE} = \frac{1}{M}\sum_{i=1}^{M}\left|\frac{\widehat{N}-N}{N}\%\right|_i \tag{10}$$

where N and $\widehat{N}$ represent the actual/experimental and predicted fatigue lives, respectively and M represents the total number of samples over which the MAPE metric is computed, $i = 1,\cdots,M$.

- Pointwise Absolute Difference (PD). It is used to quantify the capability of the model to generate physically consistent S-N behavior. Specifically, it evaluates the average pointwise deviation between the normalized (between 0 and −1) PINN-generated slope behavior and the corresponding target/reference slope behavior generated during the optimization process, as shown in Eq. (11). Smaller PD values indicate superior physical consistency of the adopted PINN configuration, and vice-versa:

$$\mathrm{PD} = \frac{1}{M}\sum_{i=1}^{M}\left|\Delta N_{Prdct}^{Norm} - \Delta N_{Ref}^{Norm}\right|_i \tag{11}$$

where ΔN_{Prdct}^{Norm} represents the normalized change between two consecutive PINN-predicted fatigue-life points, ΔN_{Ref}^{Norm} is the corresponding normalized change from the reference equation. The reference curve is also converted into ΔN and normalized before comparison, and M represents the total number of samples over which the metrics are computed, $i = 1,\cdots,M$.

The reference fatigue curve is generated using a power-law fatigue relationship obtained from experimental fatigue behavior. The reference curve is obtained using Eq. (1) for the unaged material condition (i.e., $N_0 = 8.139 \times 10^8 d^{-3.279}$) over a displacement range extending from 9 to 21 mm using 50 equally spaced displacement points.

Once the two metrics are computed on both training and validation datasets, the configurations producing the minimum average MAPE and PD values are identified and used as the reference configurations of each metric for computing the normalized MAPE and PD ratios of all investigated PINN configurations. Indeed, the configurations associated with the minimum MAPE and PD metrics obtain a ratio of 1 and all other remaining ones produce ratio values greater than 1.

Finally, the overall optimization criterion is determined by computing the average prediction-accuracy ratio and the physics-consistency ratio. The optimal configuration that produces the minimum overall ratio value is selected, thereby achieving a compromise between predictive accuracy and physical consistency of the generated S-N behavior.

In addition to the optimization criteria described above, additional statistical metrics are also computed and reported for completeness, including the Mean Absolute Error (MAE) (Eq. (12)), Root Mean Square Error (RMSE) (Eq. (13)), and Coefficient of Determination (R^2) (Eq. (14)), to provide a comprehensive assessment of the predictive capability and generalization performance of the investigated PINN configurations.

$$\mathrm{MAE} = \frac{1}{M}\sum_{i=1}^{M}|\widehat{N}-N|_i \tag{12}$$

$$\mathrm{RMSE} = \sqrt{\frac{1}{M}\sum_{i=1}^{M}\left(\widehat{N}-N\right)_i^2} \tag{13}$$

$$\mathrm{R}^2 = 1-\frac{\sum_{i=1}^{M}\left(N-\widehat{N}\right)_i^2}{\sum_{i=1}^{M}\left(N-\overline{N}\right)_i^2} \tag{14}$$

where $\overline{N}$ denotes the average experimental fatigue life.

6. Extension of ANN-based models to spectral aging conditions

Machine-learning approaches have increasingly been applied to fatigue-life prediction under variable loading histories. Previous studies have used ANN, recurrent-network, and physics-based machine-learning frameworks to represent nonlinear damage accumulation, temporal dependencies, and load-history effects under non-uniform mechanical loading [34,43,44]. In general, the available literature is primarily focused on variable or spectral mechanical loading. In contrast, no studies have been identified that address spectral TO aging representation within an ANN-based framework. In particular, there is a lack of methodologies capable of representing discrete or continuous aging spectra involving varying temperature–time combinations as direct ANN inputs for fatigue-life prediction. This gap is significant because real service environments rarely involve constant-temperature exposure, and degradation processes are inherently governed by the cumulative and history-dependent effects of variable thermal conditions.

The principal methodological contribution of this study is the development of spectral-aging representations that enable an ANN-based fatigue-life predictor trained exclusively using isothermal preaging data to predict fatigue life under multi-temperature preaging histories. The underlying predictor is assumed to accept preaging temperature, preaging duration, and fatigue displacement as inputs and to provide fatigue life as its output. Because such a model accepts only a single temperature-duration pair, it cannot directly process a preaging spectrum consisting of multiple consecutive thermal segments.

In the present study, the optimized PINN developed in Section 5 is employed as the underlying isothermal fatigue-life predictor because of its ability to generate physically consistent S-N curves. However, the spectral-aging representations introduced in this section are not inherently restricted to the adopted PINN architecture. In principle, they may be coupled with other ANN-based fatigue-life predictors having the same input–output structure and trained using isothermal preaging data.

Two different representation approaches are proposed. The first, which is analytically based, is referred to as the equivalent-aging representation. This approach transforms the complete aging spectrum into a single equivalent isothermal temperature-duration pair that can be supplied directly to the underlying ANN-based model. The second approach is referred to as the incremental-degradation representation. It preserves the individual thermal segments and evaluates them sequentially while accounting for the aging history accumulated before each segment. The following subsections present the formulation of these two approaches.

6.1. Equivalent aging representation

One possible approach for extending the applicability of the ANN-based fatigue-life model to spectral preaging conditions is to determine an equivalent single-step aging representation that produces the same effect on fatigue life as the original multi-step aging spectrum. The resulting equivalent temperature-duration pair can then be supplied directly to the underlying ANN-based without modifying or retraining its architecture.

6.1.1. Weighted-mean-temperature equivalent aging method

The first and simplest approximation assumes that the entire aging spectrum may be represented by a single equivalent constant temperature corresponding to the time-weighted average temperature of the exposure history. In this approach, the influence of the thermal spectrum is reduced to an averaged thermal exposure while preserving the total exposure duration.

For an aging spectrum consisting of n segments, the equivalent temperature can be calculated as:

$$T_{eq} = \frac{\sum_{i=1}^{n} T_i \Delta t_i}{\sum_{i=1}^{n} \Delta t_i} \tag{15}$$

where T_i is the temperature associated with segment i and Δt_i is the duration of segment i.

The equivalent aging duration is defined as the total accumulated aging duration:

$$t_{eq} = \sum_{i=1}^{n} \Delta t_i \tag{16}$$

The resulting pair of equivalent temperature and duration (T_{eq}, t_{eq}) is then directly supplied to the PINN as the preaging input condition.

This method assumes that thermal aging evolves linearly with both temperature and exposure duration. Consequently, all thermal segments contribute proportionally according to their duration, regardless of their absolute temperature level. The approach therefore neglects the nonlinear temperature dependence typically associated with thermally activated degradation mechanisms. The main advantage of this simplified approach is its straightforward implementation, as it does not require any additional material parameters. The method may provide reasonable approximations when the thermal spectrum spans a relatively narrow temperature range or when the degradation kinetics exhibit limited temperature sensitivity. However, for polymers undergoing TO aging processes, elevated temperatures generally contribute disproportionately to degradation. Under such conditions, the averaging procedure may underestimate the influence of high-temperature exposure segments, thereby reducing prediction accuracy.

6.1.2. Arrhenius-based equivalent-time method

To account for the nonlinear influence of temperature on thermal degradation, an Arrhenius-based time–temperature superposition approach is adopted. This method assumes that the dominant aging mechanism follows thermally activated kinetics and therefore evolves according to the Arrhenius relation [15,16]. Accordingly, the degradation rate is expressed as:

$$k(T) = A\exp\left(-\frac{E_a}{RT}\right) \tag{17}$$

where A is the pre-exponential factor, E_a is the activation energy, R is the universal gas constant, and T is the absolute temperature.

Unlike the mean-temperature method, this approach recognizes that the contribution of each thermal segment to material degradation is highly temperature dependent. As temperature increases, the exponential Arrhenius term causes the degradation rate to accelerate significantly. To incorporate this behavior, the thermal spectrum is transformed into an equivalent aging duration evaluated at a “selected” reference temperature T_{ref}. Each aging segment is converted into an equivalent duration at the reference temperature according to:

$$\Delta t_{\mathrm{eq},i} = \Delta t_i \exp\left[-\frac{E_a}{R}\left(\frac{1}{T_i}-\frac{1}{T_{\mathrm{ref}}}\right)\right] \tag{18}$$

The total equivalent aging duration corresponding to the spectrum can then be obtained through the accumulation of all equivalent segments as:

$$t_{\mathrm{eq}} = \sum_{i=1}^{n} \Delta t_i \exp\left[-\frac{E_a}{R}\left(\frac{1}{T_i}-\frac{1}{T_{\mathrm{ref}}}\right)\right] \tag{19}$$

The thermal spectrum is therefore represented by the equivalent aging pair T_{ref} and t_{eq}, which is supplied to the PINN in the same format as the original isothermal training data. It should be noted that the formulation assumes that a single dominant activation energy governs degradation throughout the considered temperature range. Therefore, the accuracy of the equivalent aging duration obtained from Eq. (19) depends on the accuracy of the activation energy value used in the calculations. The activation energy for NR used in the present work is adopted from Neuhaus et al. [6], where $E_a = 101.4\ \mathrm{kJ\ mol^{-1}}$.

To calculate the equivalent aging duration (t_{eq}) using this formulation, a reference temperature (T_{ref}) needs to be selected. Different choices of T_{ref} theoretically represent identical cumulative aging exposure, where the numerical value of the equivalent aging duration changes with the selected reference condition. In the present work, the reference temperature (T_{ref}) is selected from within the temperatures used during network training (i.e., 70 °C, 85 °C, 100 °C, or 120°C) in order to minimize interpolation/extrapolation effects and maintain consistency with the trained dataset. In addition, it is preferable to select T_{ref} within the central portion of the training range (i.e., 85 °C or 100 °C) where that improves numerical stability and reduces distortion in the equivalent aging duration.

This Arrhenius-based equivalent-time formulation preserves compatibility with the PINN architecture while incorporating physically meaningful thermal-aging kinetics. Compared with the mean-temperature approach, this method more accurately captures the dominant influence of elevated aging temperatures on degradation accumulation.

6.2. Incremental-degradation representation

In addition to the equivalent aging approaches described previously, a second methodology referred to as the incremental-degradation representation is proposed and investigated in this study. Unlike the equivalent-condition approaches, which reduce the entire thermal spectrum into a single representative isothermal aging condition, the present method treats each thermal segment individually and evaluates its contribution to fatigue-life degradation sequentially. The essence of this approach is to preserve the stepwise nature of the aging spectrum while maintaining compatibility with the PINN trained using discrete isothermal aging conditions.

For an aging spectrum consisting of n aging segments, each segment is characterized by its corresponding temperature T_i and duration Δt_i. The fatigue-life degradation associated with each thermal segment is represented through a "retained-life ratio" (R_L) defined as the ratio of fatigue life after the aging segment to the original life before the aging segment. Since the relationship between fatigue life and aging duration is generally nonlinear, the degradation associated with a given aging step depends on the degradation accumulated during the preceding steps. Therefore, the retained-life ratio associated with each aging step is evaluated relative to the material state existing at the beginning of that step rather than relative to the virgin material condition.

To account for the preceding aging history, the cumulative thermal exposure prior to each aging step is converted into an equivalent aging duration at the temperature of the current step using the Arrhenius time–temperature superposition formulation. For aging step i, the equivalent starting aging time at temperature T_i is denoted by $t_{i,\mathrm{eq\_start}}$. The equivalent starting time is obtained by converting each preceding aging segment into an equivalent time at temperature T_i using the Arrhenius relation:

$$t_{i,\mathrm{eq\_start}} = \sum_{j=1}^{i-1} \Delta t_j \exp\left[-\frac{E_a}{R}\left(\frac{1}{T_j} - \frac{1}{T_i}\right)\right] \tag{20}$$

where T_i is the temperature of the current aging segment, T_j and Δt_j are the temperature and the duration of a preceding aging segment j. It is worth mentioning that a single constant activation-energy value is used in Eq. (20) for this time–temperature conversion. This parameter is used only to establish the equivalent starting state of each aging step and does not directly prescribe the corresponding fatigue-life degradation, which is subsequently determined by the PINN. For the first aging segment, no preceding aging history exists and therefore $t_{1,\mathrm{eq\_start}} = 0$.

The ending time associated with aging step i is then:

$$t_{i,\mathrm{end}} = t_{i,\mathrm{eq\_start}} + \Delta t_i \tag{21}$$

where Δt_i is the actual duration of aging step i.

The PINN is subsequently used to evaluate the fatigue life at the beginning and end of each aging step. The fatigue life corresponding to the material state at the beginning of aging step i is:

$$N_{i,\mathrm{start}} = P\left(T_i, t_{i,\mathrm{eq\_start}}, d\right) \tag{22}$$

where $P(\cdot)$ denotes the prediction of the trained PINN model and d is the fatigue displacement.

Similarly, the fatigue life corresponding to the material state at the end of the same aging step is:

$$N_{i,\mathrm{end}} = P\left(T_i, t_{i,\mathrm{end}}, d\right) \tag{23}$$

The retained-life ratio associated with aging step i is consequently calculated as:

$$R_{Li} = \frac{N_{i,\mathrm{end}}}{N_{i,\mathrm{eq\_start}}} \tag{24}$$

The retained-life ratio therefore represents the relative change in fatigue-life capacity occurring during the corresponding aging step while accounting for the degradation state existing at the beginning of that step. Values of R_L smaller than unity indicate a reduction in fatigue-life capacity due to the aging step, whereas values greater than unity indicate that aging has increased the fatigue life.

The cumulative retained-life ratio ($R_{L\mathrm{cum}}$) corresponding to the complete aging spectrum is obtained by multiplying the retained-life ratios of the consecutive aging steps:

$$R_{L\mathrm{cum}} = \prod_{i=1}^{n} R_{Li} \tag{25}$$

The multiplicative form in Eq. (25) follows directly from the definition of the retained-life ratios for consecutive material states rather than representing an independently assumed damage-accumulation law. To illustrate this, consider the fatigue-life capacities associated with consecutive aging states as $N_0, N_1, \cdots, N_n$. The retained-life ratios for the consecutive states are $R_{L1} = N_1/N_0$, $R_{L2} = N_2/N_1$, …, and $R_{Ln} = N_n/N_{n-1}$. Therefore,

$$\prod_{i=1}^{n} R_{Li} = \frac{N_1}{N_0}\frac{N_2}{N_1}\cdots\frac{N_n}{N_{n-1}} = \frac{N_n}{N_0} \tag{26}$$

where the intermediate fatigue-life terms cancel.

Consequently, the predicted fatigue life corresponding to the complete aging spectrum is obtained as:

$$N_{\mathrm{spec}} = N_0 R_{L\mathrm{cum}} = N_0 \prod_{i=1}^{n} R_{Li} \tag{27}$$

where N_0 denotes the predicted fatigue life corresponding to the unaged material condition (virgin material) at the same displacement. Thus, multiplication of the consecutive retained life ratios simply provides the overall relative change in fatigue-life capacity from the initial unaged state to the final state following completion of the aging spectrum.

The principal modeling assumption in the proposed formulation is associated with the representation of the material state at the beginning of each aging step. Specifically, the cumulative TO aging from the preceding aging steps is represented by an equivalent aging duration at the temperature of the current step using the Arrhenius time–temperature relation. This assumes that the effects of preceding thermal exposures can be transformed into an equivalent thermal exposure at the current aging temperature. Importantly, the Arrhenius transformation is used only to determine the equivalent starting state of each aging step, and it does not assume a linear relationship between fatigue-life degradation and aging duration. The potentially nonlinear relationship between aging duration and fatigue life is captured through the PINN evaluations at the beginning and end of each aging step.

Recent studies on fatigue damage in metallic and solder materials have employed entropy-based, unified creep-plasticity, crystal-plasticity, and phase-field formulations to describe cumulative degradation, damage evolution, and fracture development under cyclic loading [45–48]. Although the underlying mechanisms in these materials differ from the TO aging mechanisms of NR, these studies support the broader concept that degradation evolves cumulatively and that the response to a subsequent loading or environmental increment depends on the material state established by the preceding history. Entropy-based and unified creep-plasticity damage models have shown that the loss of mechanical capacity can evolve nonlinearly and that the accumulated degradation state influences the subsequent material response [45,46]. Crystal-plasticity studies similarly relate damage evolution to accumulated internal variables, while phase-field formulations distinguish distributed scalar degradation from explicit crack localization [47,48]. In the present work, the retained-life ratio is therefore interpreted only as a macroscopic measure of the change in fatigue-life capacity between consecutive aging states and is not intended to represent a local continuum-damage variable, microstructural damage field, or explicit fracture variable.

Accordingly, the proposed incremental-degradation representation evaluates each thermal segment relative to the material state established by the preceding aging history. Unlike the equivalent-aging approaches, it does not collapse the complete spectrum into a single temperature-duration pair or require selection of a global reference temperature. The formulation operates externally to the underlying fatigue-life predictor and therefore requires no network modification or retraining. Although implemented here using the optimized PINN, it can in principle be coupled with other ANN-based models trained using isothermal preaging data and having the same input–output structure.

7. Results and discussion

In this section, the results of the PINN optimization study are first presented to identify the network architecture and training parameters that provide the best predictive performance based on the training and validation datasets. The influence of the investigated hyperparameters on model accuracy and generalization capability is examined, and the optimal PINN configuration is subsequently selected. The predictive performance of the optimized PINN is then evaluated using the testing dataset and compared against the corresponding experimental fatigue-life data under isothermal conditions. Finally, the proposed equivalent-aging and incremental-degradation representations are assessed for the spectral preaging condition and compared with experimental data and the analytical Neuhaus model.

The development, optimization, and implementation of the PINN models presented in this study were carried out using MATLAB®. Models were executed using a personal computer equipped with a 13th-generation Intel® Core™ i5-1335U processor. This computational setup was sufficient to support the computations described in this study with no computational limitations affecting the reported results.

7.1. Model optimization results

Among the 240 PINN configurations investigated according to Section 5.3, the minimum average MAPE is achieved for Configuration #226, characterized by 19 hidden neurons, a LeakyReLU activation function, and the Adam optimizer. This configuration produced an average MAPE value of 18.85% and therefore serves as the reference configuration for the fatigue life prediction-accuracy metric. Fig. 3 shows the PINN generated S-N curves for Configuration #226 under preaging conditions 1–4. As can be seen in Fig. 3, the generated S-N curves exhibit local oscillations and non-uniform curvature, deviating from the smooth monotonic power-law trend expected for fatigue-life relationships. Such deviations clearly indicate that minimizing the prediction error alone does not produce physically realistic fatigue behavior.

Conversely, the minimum PD value is obtained for Configuration #61, which is characterized by 6 hidden neurons, a Sigmoid activation function, and the Adam optimizer. This configuration produced the lowest PD value (0.0191) and therefore served as the reference configuration for the physics-consistency metric. Fig. 4 shows the S-N curves for Configuration #61 under preaging conditions 1–4. As can be seen in Fig. 4, the generated S-N curves exhibit very smooth monotonic behavior and closely follow the expected fatigue-life trend. However, despite its superior physics consistency in terms of S-N curve smoothness, its prediction accuracy is relatively poor, with a MAPE of 24.62%, clearly higher than the 18.85% obtained for Configuration #226.

To balance the competing objectives of prediction accuracy and physics-consistency, as described previously in Section 5.3, an overall optimization criterion is adopted. The overall ratio is determined by averaging the prediction-accuracy ratio and the physics-consistency ratio, thereby assigning equal importance to both objectives. The configuration producing the minimum overall ratio is then selected as the optimal PINN architecture.

Among all investigated configurations, Configuration #76 yielded the lowest overall ratio value of 1.123 and is therefore selected as the final model. This configuration is characterized by 7 hidden neurons, the tanh activation function, and the Adam optimizer, producing a PD value of 0.0223 and an average MAPE value of 20.31%. Although neither metric individually achieves the minimum value, both remained close to their respective optimum values. Consequently, based on the multi-objective optimization procedure implemented herein, Configuration #76 provides the best compromise between predictive accuracy and physics consistency.

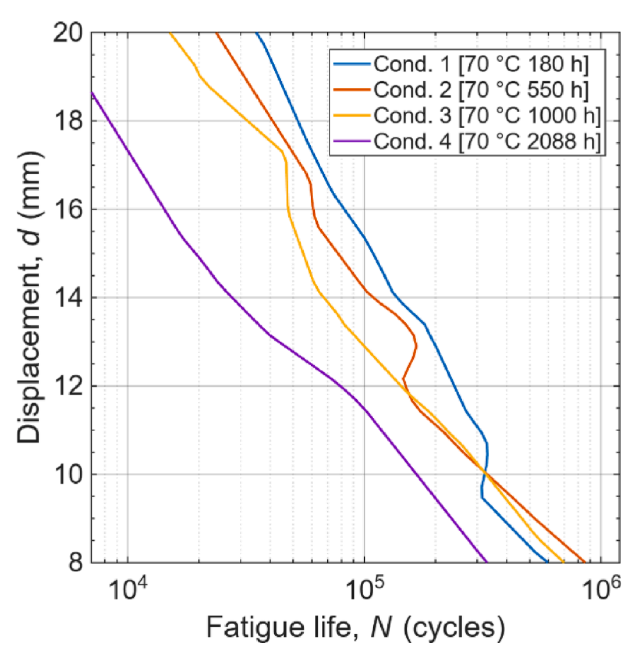

Fig. 3. Exemplary generated S-N curves for Configuration #226 (it has the lowest MAPE value) under preaging conditions 1–4.

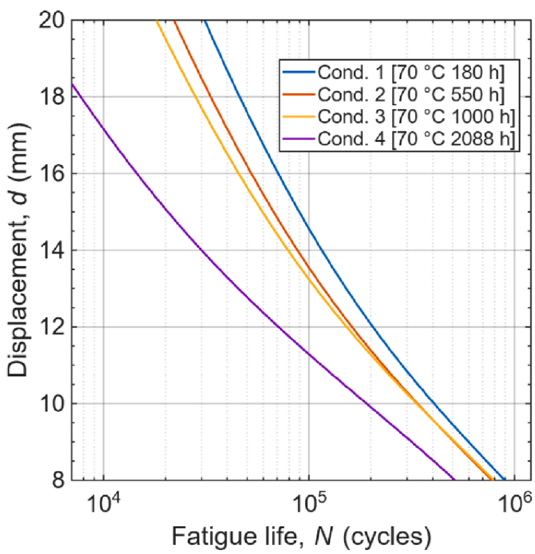

Fig. 4. Exemplary generated S-N curves for Configuration #61 (it has the lowest PD value) under preaging conditions 1–4.

Table 3 summarizes the three representative configurations. Configuration #226 minimizes prediction error, Configuration #61 provides the lowest PD, and Configuration #76 produces the lowest overall ratio. The latter is therefore selected as the optimal compromise between prediction accuracy and physical consistency.

The code corresponding to the optimal PINN configuration is provided as Supplementary Material to facilitate reproducibility and support the practical implementation of the proposed framework. Readers may use the supplied code to generate fatigue-life predictions for new aging and testing conditions within the range of the training data, as well as for conditions involving limited extrapolation beyond this range. The provided implementation can also serve as a basis for further investigation, validation, and extension of the developed model.

7.2. PINN predictions for testing dataset

The generalization capability of the optimized PINN is next evaluated using the testing subsets under increasingly complex aging conditions. As stated earlier in Section 4, the testing subgroups considered in this study are: (i) unseen data points corresponding to the unaged condition and the isothermal preaging conditions (1) to (16) (see Table 1), (ii) data points corresponding to the two LOCs not used during training (i.e., preaging conditions (17) and (18), and (iii) data points corresponding to the spectral preaging condition (Table 2). The results for each of these three subgroups are presented and discussed in the following subsections.

7.2.1. Isothermal aging conditions

The first testing subgroup represents the first level of generalization assessment. It includes datapoints having the same preaging temperatures and durations as those used during network training, but with different displacement values (loading levels). The accuracy of the PINN predictions is first evaluated using the experimental datapoints in this testing subgroup, and the resulting error metrics are: MAPE = 16.5%, MAE = 2.12×10^4 cycles, RMSE = 4.29×10^4 cycles, and $R^2 = 0.915$. Given the highly scattered nature of the fatigue-life data, these metrics indicate excellent predictive performance of the developed PINN model.

The PINN is also used to generate S-N curves for the unaged material (also referred to as the reference condition) and preaging conditions 1–16 (listed in Table 1). For each condition, the S-N curve is generated using 50 equally spaced points covering a displacement range extending from 20% below the corresponding minimum experimental displacement to 20% above the corresponding maximum experimental displacement. This displacement range intentionally exceeds the limits of the training domain in order to assess the extrapolation capability of the network. Fig. 5 shows a representative set of PINN-generated S-N curves for selected testing conditions, together with the corresponding experimental datapoints from the testing dataset. The group of curves shown in the figure corresponds to the unaged (virgin) NR condition and preaging conditions 5–9. The figure shows that, in general, preaging reduces the fatigue life of NR, with a clear reduction in life observed as the aging duration increases. However, it should also be noted that at small displacement values, preaging initially tends to increase fatigue life for short aging durations, after which the fatigue life begins to decrease. The figure further shows that the effect of aging duration on fatigue life depends on the fatigue loading level (i.e., displacement value). This is evident from the changing slopes of the S-N curves, where the absolute value of the slope decreases with increasing aging duration.

According to the Pearson correlation results presented in Section 5.1, preaging duration has the second strongest influence on fatigue life. To further investigate this effect based on the PINN predictions, the ratio of fatigue life after preaging to that of the unaged material is plotted as a function of aging duration. Since this effect is clearly dependent on the

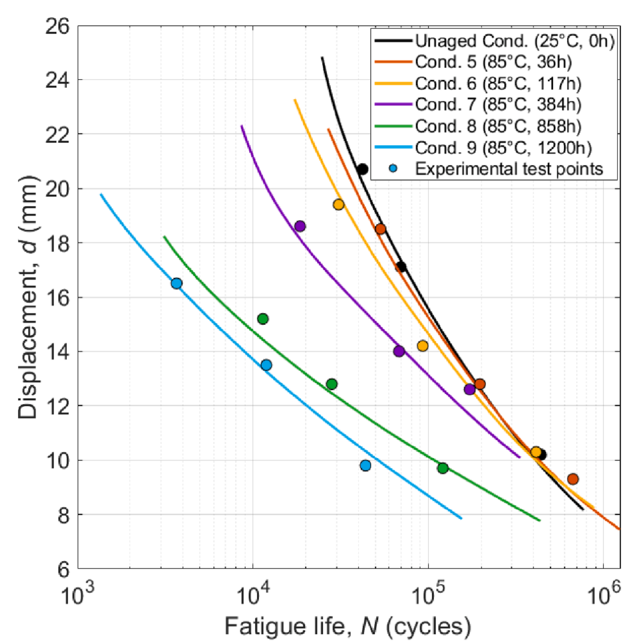

Fig. 5. Exemplary PINN-generated S-N curves for NR preaged at 85°C for different durations (with corresponding experimental datapoints from testing dataset).

Table 3
Summary of the best-performing PINN configurations identified during the optimization study.

Selection criteria	Configuration ID	Hidden neurons	Activation function	Optimizer	MAPE (%)	PD	Ratio
MAPE	226	19	Leaky ReLU	Adam	18.85	0.0463	2.304
PD	61	6	Sigmoid	Adam	24.62	0.0191	1.153
Minimum overall ratio (*optimal – selected PINN*)	76	7	tanh	Adam	20.31	0.0223	1.123

loading level, as evident by the changing slopes of the S-N curves in Fig. 5, the ratio is calculated at three displacement values (10, 15, and 20 mm), representing low, medium, and high fatigue loading levels, respectively. Fig. 6(a)–(d) shows the resulting life-ratio curves as a function of preaging duration for preaging temperatures of 70 °C, 85 °C, 100 °C, and 120 °C, respectively. Each subfigure uses a different time scale, and the aging durations included in the training dataset (see Table 1) are indicated by the black vertical dashed lines. All curves begin at a life ratio of unity at zero aging duration (i.e., no preaging). The ratio then evolves with increasing aging duration, where values greater than unity indicate an improvement in fatigue life relative to the unaged condition, while values less than unity indicate degradation. The figure clearly shows that for low displacement values (i.e., $d = 10$ mm), the life ratio initially increases with aging duration before decreasing at a diminishing rate. This observation suggests that short preaging durations improve the fatigue behavior of NR at low loading levels. In contrast, for medium and high loading levels (i.e., d = 15 and 20 mm), the life ratio mostly remains below unity and decreases continuously with increasing aging duration. It should be noted that the curves corresponding to preaging at 70 °C in Fig. 6(a) exhibit a slightly different trend from those shown in the other subfigures. For example, the curve corresponding to d = 10 mm shows multiple local decreases and increases. By examining the aging durations included in the training dataset, it can be seen that the nonphysical behavior occurs in the intermediate regions between the available training points. Specifically, the nonphysical fluctuations appear between approximately 550 h and 1000 h and between 1000 h and 2088 h, where no training data are available. From a modeling perspective, this behavior is indicative of local overfitting and may reduce the predictive accuracy of the PINN within these interpolation intervals. The most likely cause is the relatively large gaps between the aging durations represented in the training dataset, which provide insufficient information to adequately constrain the network response in these regions. A potential remedy would be to augment the training dataset with artificially generated physics-consistent samples in these intermediate aging-duration ranges, thereby providing additional guidance to the network while preserving the underlying physical trends. Such physics-informed data augmentation has recently been shown to improve fatigue-life prediction models without requiring additional experimental measurements [49]. However, the implementation and evaluation of such augmentation

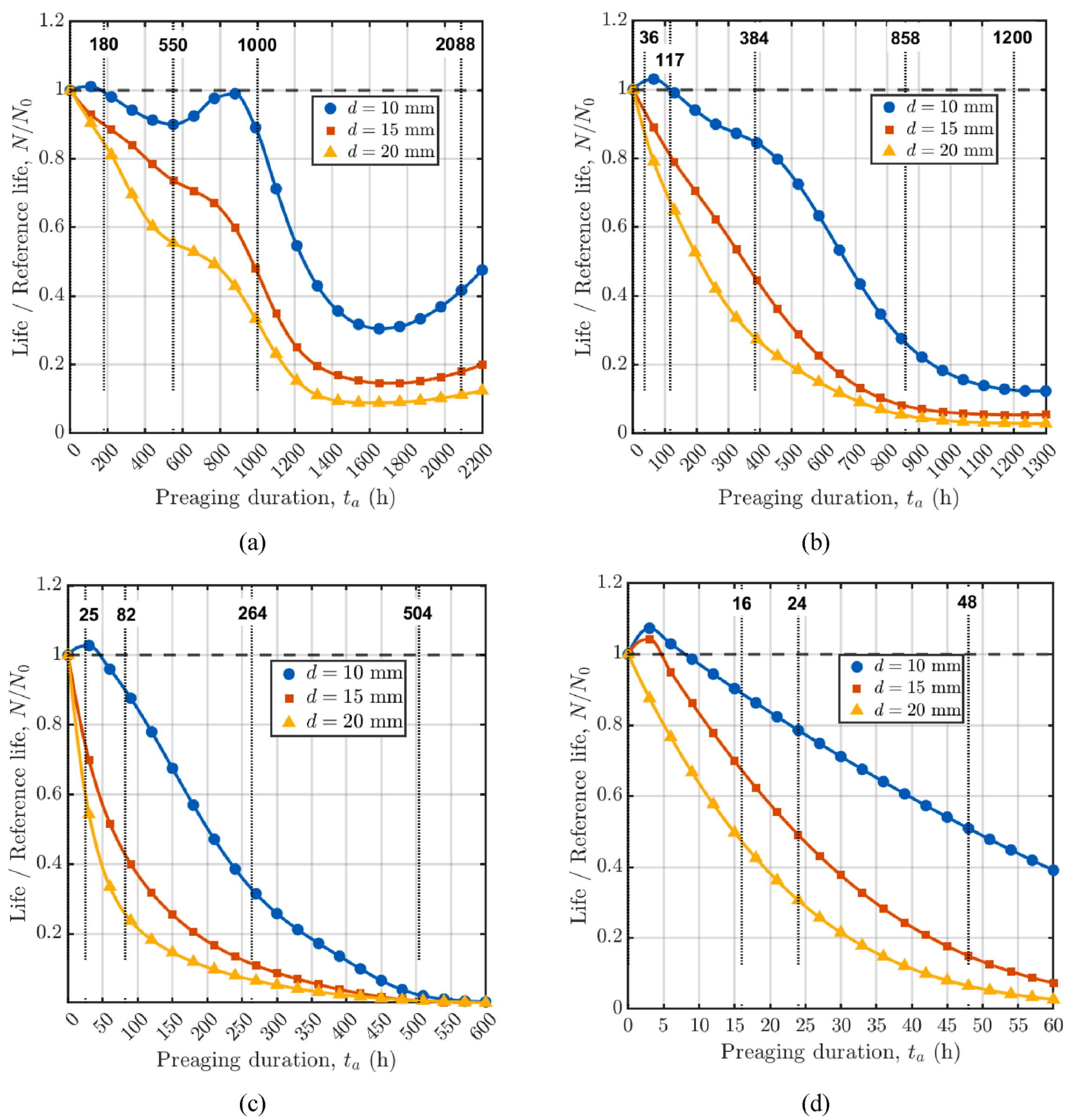

Fig. 6. Effect of preaging duration on life ratio of NR at different preaging temperatures: (a) 70°C, (b) 85°C, (c) 100°C, and (d) 120°C.

strategies are beyond the scope of the present study.

7.2.2. Left-out isothermal aging conditions

The second testing subgroup represents the next level of generalization assessment, where the PINN is used to predict the fatigue life for the two LOCs that were not used during training (conditions (17) and (18) listed in Table 1). The datapoints in this subgroup have the same preaging temperatures as those used during network training, but both the preaging durations and displacement values are different.

The datapoints corresponding to the two LOCs are used to generate experimental S-N curves by fitting a power-law relation to each condition. The resulting "experimental" S-N curves for the two LOCs are: $N_{17} = [8.39 \times 10^9] d^{-4.285}$ for preaging at 85 °C for 180 h (i.e., cond. 17) and $N_{18} = [8.02 \times 10^{10}] d^{-5.301}$ for preaging at 100 °C for 120 h (i.e., cond. 18). Fig. 7(a) and (b) show the experimental S-N curves (dashed lines), together with the datapoints used to generate them, as well as the corresponding PINN-generated S-N curves for conditions (17) and (18), respectively. The figure shows that the PINN-generated S-N curve closely matches the experimental curve for condition (17). For condition (18), the agreement is not as close, although it remains reasonably good.

Since the experimental datapoints exhibit considerable scatter, the error metrics for the PINN-generated S-N curves are calculated relative to the fitted experimental S-N curves rather than the individual datapoints. This approach provides a more representative assessment of the prediction accuracy. The error metrics for the two LOCs are calculated for d ranging from 9 to 21 mm, and they are found to be: MAPE = 6.8%, MAE = 1.2×10^4 cycles, RMSE = 2.28×10^4 cycles, and $R^2 = 0.981$ for condition (17) and MAPE = 22.7%, MAE = 2.57×10^4 cycles, RMSE = 4.08×10^4 cycles, and $R^2 = 0.939$ for condition (18). While when calculated with respect to the experimental datapoints, the error metrics are: MAPE = 7.96%, MAE = 1.6×10^4 cycles, RMSE = 2.7×10^4 cycles, and $R^2 = 0.969$ for condition (17) and MAPE = 21.95%, MAE = 1.8×10^4 cycles, RMSE = 2.3×10^4 cycles, and $R^2 = 0.951$ for condition (18). Although the MAPE value for condition (18) appears relatively high compared with that of condition (17), it remains well within the range typically considered acceptable for fatigue-life predictions and is comparable to the MAPE obtained for the first testing subgroup. Overall, the average MAPE for the two LOCs considered here is 14.8%, indicating predictive accuracy that is even slightly better than that obtained for the first testing subgroup.

7.2.3. Spectral aging conditions

The first two testing subgroups establish the predictive accuracy and generalization capability of the PINN for isothermal aging conditions. Having established this baseline performance, the final testing subgroup evaluates the ability of the proposed approaches for extending the isothermally trained PINN to the spectral preaging condition listed in Table 2. Because the underlying PINN accepts only a single preaging temperature-duration pair, the spectral history is represented using the methodologies introduced in Section 6. The resulting predictions therefore primarily assess the effectiveness of these spectral-aging representations rather than the baseline isothermal predictive capability of the PINN.

Similar to the previous section, a power-law relation is fitted to the experimental datapoints corresponding to the multi-step preaging condition considered here. The error metrics for the different PINN-generated S-N curves are then calculated relative to the fitted experimental S-N curve rather than the individual datapoints. This approach provides a more representative assessment of the prediction accuracy by minimizing the influence of the experimental scatter. The resulting experimental S-N curve is given by: $N_{spec} = [2.89 \times 10^{10}] d^{-4.926}$.

7.2.3.1. Spectrum Equivalent-Aging representation. The two equivalent-aging methods presented in Section 6.1 are applied to the multi-step aging spectrum listed in Table 2. For the weighted-mean-temperature method, the equivalent temperature and duration are calculated using Eqs. (15) and (16), respectively. The resulting equivalent aging condition is found to be $T_{eq} = 76.8^{\circ}$C and $t_{eq} = 446.8$h. For the Arrhenius-based method, on the other hand, the equivalent aging duration is calculated using Eq. (19) for a selected reference temperature. As mentioned earlier, two reference temperatures (85 °C and 100 °C) are considered for comparison purposes, as they lie near the middle of the temperature range investigated experimentally. Accordingly, the two resulting equivalent aging durations are found to be $t_{eq} = 446$h for $T_{ref} = 85^{\circ}$C and $t_{eq} = 113.5$h for $T_{ref} = 100^{\circ}$C.

Fig. 8 shows the experimental S-N curve (dashed line), together with the datapoints used to generate it, as well as the corresponding PINN-generated S-N curves obtained using the different equivalent aging temperatures and durations. It can be seen that the PINN-generated S-N curve based on the weighted-mean-temperature method clearly over-predicts the fatigue life, particularly at high displacement levels. This is expected because the weighted-mean-temperature method assumes that thermal aging evolves linearly with both temperature and exposure duration. However, the PINN predictions presented in Fig. 6 clearly demonstrate that the influence of aging duration on fatigue-life degradation is highly nonlinear. Consequently, the weighted-mean-

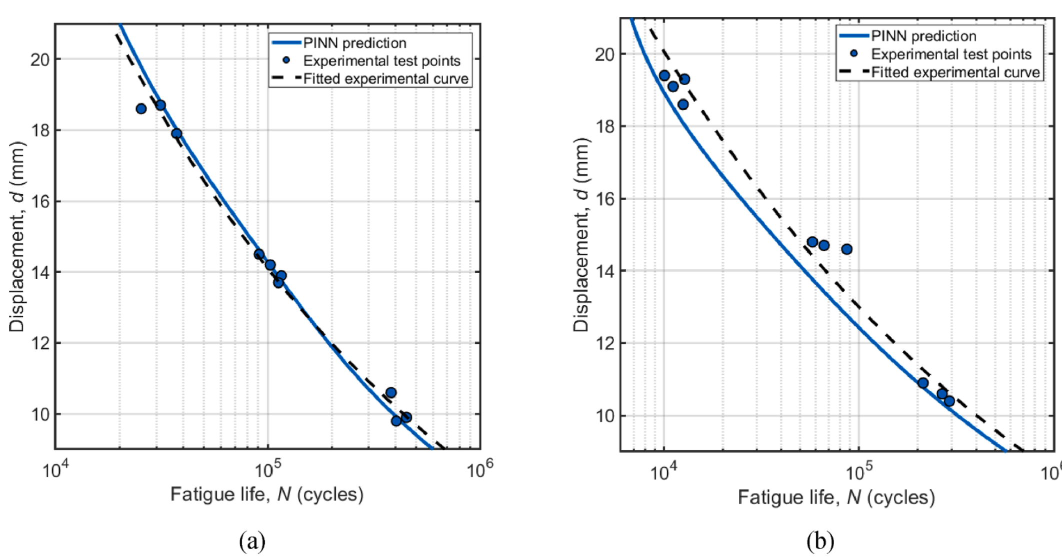

Fig. 7. Experimental and PINN-generated S-N curves for the two LOCs: (a) Cond. 17 – preaging for 180 h at 85°C and (b) Cond. 18 – preaging for 120 h at 100°C.

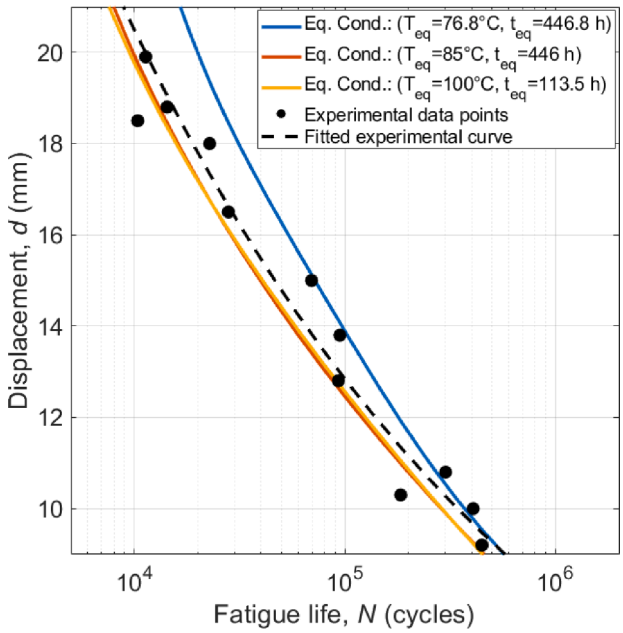

Fig. 8. Experimental S-N curve for spectrally aged specimens along with PINN-generated curves based on the different equivalent temperature-duration representations.

temperature method fails to adequately represent the cumulative effect of the thermal spectrum and produces large prediction errors with MAPE = 49.5%, MAE = 2.8×10^4 cycles, RMSE = 3.3×10^4 cycles, and $R^2 = 0.943$ with respect to the experimental curve.

The figure also shows that the S-N curves generated using the Arrhenius-based equivalent-time method slightly underpredict the fatigue life, and the deviation becomes more noticeable at higher displacement values. For $T_{ref} = 85^\circ$C, the resulting errors are MAPE = 14.64%, MAE = 1.79×10^4 cycles, RMSE = 3.1×10^4 cycles, and $R^2 = 0.949$ with respect to the experimental curve. While for $T_{ref} = 100^\circ$C, the resulting errors are MAPE = 14.24%, MAE = 1.67×10^4 cycles, RMSE = 3.12×10^4 cycles, and $R^2 = 0.95$ with respect to the experimental curve. Compared with the weighted-mean-temperature method, the Arrhenius-based method provides more conservative fatigue-life predictions and therefore offers a more reliable representation of the spectral aging condition.

Although the Arrhenius-based equivalent-time method theoretically represents the same cumulative aging exposure regardless of the selected reference temperature, the PINN predicts slightly different fatigue lives for the equivalent aging conditions obtained using reference temperatures of 85°C and 100°C. This difference arises because the physics incorporated into the PINN constrains the fatigue load-life relationship, but it does not enforce the Arrhenius time–temperature equivalence. The Arrhenius transformation is introduced only during the preprocessing of the aging inputs and is not embedded as a physical constraint during network training. Consequently, temperature–time pairs that are theoretically equivalent according to the Arrhenius relation do not necessarily produce identical fatigue-life predictions. This observation highlights a limitation of equivalent-aging representations and confirms the need for more advanced spectral aging representations that reduce, or ideally eliminate, the dependence on the selected reference temperature.

7.2.3.2. Spectrum incremental-degradation representation. The proposed incremental-degradation representation treats each thermal segment of the aging spectrum individually and evaluates its contribution to fatigue-life degradation sequentially while accounting for the aging history accumulated during the preceding steps. This approach preserves the stepwise nature of the aging spectrum while maintaining compatibility with the PINN trained exclusively using isothermal aging conditions.

The incremental-degradation formulation presented in Section 6.2 is applied sequentially to the four thermal segments listed in Table 2. Table 4 lists the calculated equivalent starting and ending times for each of the four aging steps considered in the experimental spectrum. For the first aging step, no preceding aging history exists and the equivalent starting time is therefore zero. For each subsequent step, the equivalent starting time incorporates the cumulative exposure from all preceding aging steps transformed to the temperature of the current step. Since the retained life ratio for each step is determined from the fatigue lives at both the beginning and end of that step, two PINN evaluations are required per aging step. Consequently, for the four-step aging spectrum considered here, the PINN is evaluated a total of eight times using the conditions listed in Table 4. After evaluating the retained life ratio for each aging step, the cumulative retained life ratio corresponding to the complete aging spectrum is calculated using Eq. (25). Finally, the fatigue life corresponding to the complete spectrum is then determined using Eq. (27).

Fig. 9 shows the experimental S-N curve (dashed line), together with the datapoints used to generate it, as well as the corresponding PINN-generated S-N curves for the unaged (virgin) material (solid black line), the individual preaging steps, and the complete preaging spectrum. Also, for comparison, the fatigue-life predictions obtained using the analytical formulation of Neuhaus et al. [6] using both constant and adapted variable values of the activation energy are included in Fig. 9. The S-N curves corresponding to the individual preaging steps illustrate the relative change in fatigue-life capacity associated with each step, as determined from its retained life ratio. It can be seen from the figure that the four preaging steps have a similar influence on fatigue life, as evidenced by the close proximity of the corresponding S-N curves. This observation is consistent with the theoretical analysis reported by Neuhaus et al. [6].

The figure clearly shows that the PINN-generated S-N curve obtained using the proposed incremental-degradation representation for the complete preaging spectrum is in excellent agreement with the experimental S-N curve. Similar to the case of the LOCs, the error metrics are calculated relative to the fitted experimental curve (not the experimental datapoints) for d ranging between 9 and 21 mm. The resulting error metrics are MAPE = 6.13%, MAE = 1.19×10^4 cycles, RMSE = 2.51×10^4 cycles, and $R^2 = 0.97$ with respect to the experimental curve (MAPE = 20.26%, MAE = 2.86×10^4 cycles, RMSE = 4.73×10^4 cycles, and $R^2 = 0.903$ with respect to the experimental datapoints). These errors are comparable to, or lower than, those obtained for the isothermal testing subsets, demonstrating that the proposed representation successfully extends the isothermally trained PINN to the investigated spectral condition.

Fig. 9 also highlights an important limitation of the Neuhaus analytical formulation when a single average activation energy is employed. Under this assumption, the predicted S-N curve retains approximately the same slope as the unaged curve and therefore does not accurately reproduce the experimentally observed change in S-N slope. This results in relatively high errors where MAPE = 36.34% and

Table 4
The PINN inputs for preaging spectrum steps with equivalent starting and ending times.

Step ID	PINN Stepwise Preaging Inputs		
	Temp., T_i	Equiv. Start Time, $t_{i,\mathrm{eq\_start}}$	End Time, $t_{i,\mathrm{end}}$
	(°C)	(hour)	(hour)
A	70	0	287.4
B	85	64.95	192.25
C	100	48.97	73.47
D	120	13.92	21.52

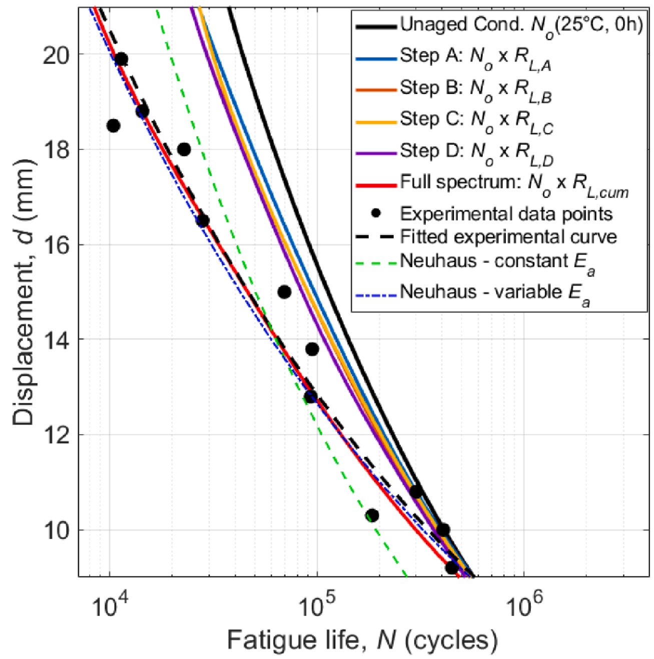

Fig. 9. Experimental S-N curve for spectrally aged specimens together with predictions obtained using the proposed PINN-based incremental-degradation representation and the analytical model of Neuhaus et al. [6].

MAE = 7.99×10^4 cycles. In contrast, allowing the activation energy to vary with both preaging temperature and displacement enables the analytical prediction to reproduce the slope change and results in close agreement with the experimental curve (MAPE = 8.4%, MAE = 1.26×10^4 cycles, RMSE = 2.9×10^4 cycles, and $R^2 = 0.994$). However, determination of these variable activation-energy values requires a relatively lengthy calibration procedure involving identification of characteristic aging times at multiple temperature-displacement combinations followed by separate Arrhenius fits.

It should be noted here that the proposed incremental-degradation approach employs constant activation energy; however, its role is fundamentally different from that in the Neuhaus analytical model. The activation energy is employed only for converting the preceding thermal history into an equivalent starting time at the temperature of each subsequent aging step. The corresponding fatigue-life change is then determined by the PINN from the nonlinear behavior learned using isothermal experimental data. Thus, the constant activation energy is used to represent the thermal-history equivalence between consecutive steps rather than to directly prescribe the magnitude of fatigue-life degradation. This allows the incremental-degradation approach to capture the correct S-N behavior without requiring explicit determination of temperature and displacement dependent activation energy values.

The principal practical advantage of the incremental-degradation representation is therefore its ability to preserve the nonlinear, stepwise evolution of fatigue-life capacity while remaining compatible with an ANN trained exclusively using isothermal aging data. The results of the investigated four-step spectrum demonstrate the potential of the proposed methodology for extending an isothermally trained PINN to multi-temperature preaging histories. However, the experimental validation available in the present study is limited to the single increasing-temperature spectrum listed in Table 2. Therefore, the present results should be interpreted as validation of the proposed approach for the investigated spectrum rather than as confirmation of its predictive accuracy for arbitrary temperature sequences and duration combinations. Further experimental investigation involving different temperature sequences and aging durations would be valuable for assessing the broader generalization capability of the proposed methodology.

Although the methodology proposed in this study has been developed and partially validated for multi-temperature TO preaging histories, its underlying concept is considerably more general. The concept is based on representing a complex loading or environmental history as a sequence of simpler states that can be evaluated individually using a network trained under well-defined conditions. Consequently, the proposed methodology can potentially be extended to other fatigue problems involving sequential degradation processes, such as variable-amplitude fatigue loading, combined mechanical and environmental loading, or other multi-physics aging scenarios.

8. Concluding remarks

This study presents an ANN-based framework for predicting the fatigue life of natural rubber subjected to thermo-oxidative preaging spectra. The proposed methodology extends ANN-based fatigue-life prediction from isothermal preaging conditions to multi-temperature preaging histories through the introduction of a novel spectral-aging representation. Consequently, complex spectral aging histories become compatible with networks trained exclusively using isothermal aging data. Based on the obtained results, the following conclusions can be drawn:

- The proposed PINN combines data-driven learning with a simple physics-based constraint to achieve accurate and physically consistent fatigue-life predictions while preserving the expected monotonic power-law S-N behavior.
- The proposed multi-objective optimization procedure balances prediction accuracy and physical consistency to identify an optimal PINN architecture and avoid unrealistic S-N behavior that may arise when optimization relies only on conventional error metrics.
- The optimized PINN provides accurate and physically consistent fatigue-life predictions for isothermal preaging conditions, including unseen datapoints and left-out aging conditions.
- The Arrhenius-based equivalent-time representation provides substantially better spectral-aging predictions than the weighted-mean-temperature method, although its predictions remain dependent on the selected reference temperature.
- The proposed incremental-degradation representation provides the highest spectral-aging accuracy, with a MAPE of 6.13%, by evaluating the individual thermal segments sequentially while accounting for the preceding aging history.
- The Neuhaus analytical model reproduces the experimental change in S-N slope only when activation energy is allowed to vary with both preaging temperature and displacement. Although this produces accurate predictions, determination of the required variable activation-energy parameters involves extensive calibration. In contrast, the proposed incremental approach uses a constant activation energy only for thermal-history conversion while allowing the PINN to determine the nonlinear fatigue-life degradation.
- The proposed spectral-aging representation operates externally to the underlying ANN and requires no retraining, providing a general strategy for extending ANN-based predictors trained under isothermal conditions to more complex cumulative histories.

Overall, the proposed framework provides a practical means of extending ANN-based fatigue-life models trained using isothermal preaging data to multi-temperature aging histories without requiring spectral-aging data during network training.

Declaration of the use of artificial intelligence

During the preparation of this work, the authors used generative AI to improve the language, readability, and presentation of the manuscript and to assist in identifying relevant literature for the literature review.

After using this tool, the authors carefully reviewed, edited, and verified all generated content and independently assessed the relevance and accuracy of the cited literature. The authors take full responsibility for the content of the published work.

CRediT authorship contribution statement

Ala Hijazi: Writing – original draft, Validation, Methodology, Investigation, Formal analysis, Data curation, Conceptualization. **Sameer Al-Dahidi:** Visualization, Software, Methodology, Investigation, Formal analysis.

Declaration of competing interest

The authors declare that they have no known competing financial interests or personal relationships that could have appeared to influence the work reported in this paper.

Acknowledgements

The first author acknowledges financial support from the German Jordanian University during his sabbatical leave and the hospitality and support of Istanbul Gelisim University.

Appendix A. Supplementary material

Supplementary data to this article can be found online at https://doi.org/10.1016/j.ijfatigue.2026.109952.

Data availability

Data will be made available on request.

References

[1] Kim WD, Lee HJ, Kim JY, Koh SK. Fatigue life estimation of an engine rubber mount. Int J Fatigue 2004;26(5):553–60.
[2] Ayoub G, Naït-Abdelaziz M, Zaïri F. Multiaxial fatigue life predictors for rubbers: application of recent developments to a carbon-filled SBR. Int J Fatigue 2014;66:168–76.
[3] Le Cam JB, Huneau B, Verron E. Fatigue damage in carbon black filled natural rubber under uni-and multiaxial loading conditions. Int J Fatigue 2013;52:82–94.
[4] Gehling T, Schieppati J, Balasooriya W, Kerschbaumer RC, Pinter G. Fatigue behavior of elastomeric components: a review of the key factors of rubber formulation, manufacturing, and service conditions. Polym Rev 2023;63(3):763–804.
[5] Bensalem K, Eesaee M, Hassanipour M, Elkoun S, David E, Agbossou K, et al. Lifetime estimation models and degradation mechanisms of elastomeric materials: a critical review. Polym Degrad Stab 2024;220:110644.
[6] Neuhaus C, Lion A, Johlitz M, Heuler P, Barkhoff M, Duisen F. Fatigue behaviour of an elastomer under consideration of ageing effects. Int J Fatigue 2017;104:72–80.
[7] Cadwell SM, Merrill RA, Sloman CM, Yost FL. Dynamic fatigue life of rubber. Rubber Chem Technol 1940;13(2):304–15.
[8] Duan X, Shangguan WB, Li M, Rakheja S. Measurement and modelling of the fatigue life of rubber mounts for an automotive powertrain at high temperatures. Proc Inst Mech Eng Part D: J Auto Eng 2016;230(7):942–54.
[9] Abdelmoniem M, Yagimli B. Self-heating in rubber components: experimental studies and numerical analysis: M. Abdelmoniem, B. Yagimli. J Rubber Res 2025;28(1):71–85.
[10] Lake GJ, Lindley PB. Cut growth and fatigue of rubbers. II. Experiments on a noncrystallizing rubber. J Appl Polym Sci 1964;8(2):707–21.
[11] Ruellan B, Le Cam JB, Jeanneau I, Canévet F, Mortier F, Robin E. Fatigue of natural rubber under different temperatures. Int J Fatigue 2019;124:544–57.
[12] Celina MC. Review of polymer oxidation and its relationship with materials performance and lifetime prediction. Polym Degrad Stab 2013;98(12):2419–29.
[13] Audouin L, Langlois V, Verdu J, De Bruijn JCM. Role of oxygen diffusion in polymer ageing: kinetic and mechanical aspects. J Mater Sci 1994;29(3):569–83.
[14] Abdelaziz MN, Ayoub G, Colin X, Benhassine M, Mouwakeh M. New developments in fracture of rubbers: predictive tools and influence of thermal aging. Int J Solids Struct 2019;165:127–36.
[15] Arrhenius S. Über die Reaktionsgeschwindigkeit bei der Inversion von Rohrzucker durch Säuren. Zeitschrift für physikalische Chemie 1889;4(1):226–48.
[16] Wise J, Gillen KT, Clough RL. An ultrasensitive technique for testing the Arrhenius extrapolation assumption for thermally aged elastomers. Polym Degrad Stab 1995;49(3):403–18.
[17] Ferry JD. Viscoelastic Properties of Polymers. 3rd Ed. Wiley; 1980.
[18] Haykin S. Neural Networks: A Comprehensive Foundation. Prentice Hall PTR; 1998.
[19] Pestana MS, Kalombo RB, Freire Júnior RCS, Ferreira JLA, da Silva CRM, Araújo JA. Use of artificial neural network to assess the effect of mean stress on fatigue of overhead conductors. Fatigue Fract Eng Mater Struct 2018;41(12):2577–86.
[20] Kalombo RB, Pestana MS, Júnior RF, Ferreira JLA, Silva CRM, Veloso LACM, et al. Fatigue life estimation of an all aluminum alloy 1055 MCM conductor for different mean stresses using an artificial neural network. Int J Fatigue 2020;140:105814.
[21] Sun H, Qiu Y, Li J. A novel artificial neural network model for wide-band random fatigue life prediction. Int J Fatigue 2022;157:106701.
[22] Xiang KL, Xiang PY, Wu YP. Prediction of the fatigue life of natural rubber composites by artificial neural network approaches. Mater Des 2014;57:180–5.
[23] Chen J, Liu Y. Fatigue modeling using neural networks: a comprehensive review. Fatigue Fract Eng Mater Struct 2022;45(4):945–79.
[24] Liu X, Zhao X, Shangguan WB. Fatigue life prediction of natural rubber components using an artificial neural network. Fatigue Fract Eng Mater Struct 2022;45(6):1678–89.
[25] Robin E, Le Cam J, Delahaye G, Ruellan B, Di Cesare N, Canévet F. A first proposal for fatigue life prediction of carbon black filled natural rubber at different temperatures with an artificial neural network. Strain 2025;61.
[26] Sun Y, Liu X, Yang Q, Liu X, He K. Improving fatigue life prediction of natural rubber using a physics-informed neural network model. Fatigue Fract Eng Mater Struct 2025;48(3):1039–49.
[27] Liu Y, Shangguan WB, Liu X, Qian X. Physics-informed neural network model for predicting the fatigue life of natural rubber under ambient temperature effects. Fatigue Fract Eng Mater Struct 2025.
[28] Li QQ, Xu ZD, Dong YR, He JX, Tian Y, He ZH, et al. Mechanical property tests and physics-informed data-driven modeling of viscoelastic materials subjected to thermal-oxidative aging. Constr Build Mater 2024;414:134920.
[29] Hijazi A, Al-Dahidi S, Lion A. Neural networks-based fatigue life prediction of natural rubber under combined preaging and temperature effects. Contin Mech Thermodyn 2026;38(3):42.
[30] Neuhaus, C. (2019). Methodenentwicklung für die Lebensdaueruntersuchung thermomechanisch beanspruchter Elastomerlager. Ph.D. thesis, Universität der Bundeswehr München.
[31] Psichogios DC, Ungar LH. A hybrid neural network-first principles approach to process modeling. AIChE J 1992;38(10):1499–511.
[32] Raissi M, Perdikaris P, Karniadakis GE. Physics-informed neural networks: a deep learning framework for solving forward and inverse problems involving nonlinear partial differential equations. J Comput Phys 2019;378:686–707.
[33] Hijazi A, Al-Dahidi S, Altarazi S. A novel assisted artificial neural network modeling approach for improved accuracy using small datasets: application in residual strength evaluation of panels with multiple site damage cracks. Appl Sci 2020;10(22):8255.
[34] Baktheer A, Aldakheel F. Physics-based machine learning for fatigue lifetime prediction under non-uniform loading scenarios. Comput Methods Appl Mech Eng 2025;444:118116.
[35] Karniadakis GE, Kevrekidis IG, Lu L, Perdikaris P, Wang S, Yang L. Physics-informed machine learning. Nat Rev Phys 2021;3(6):422–40.
[36] Cuomo S, Di Cola VS, Giampaolo F, Rozza G, Raissi M, Piccialli F. Scientific machine learning through physics–informed neural networks: where we are and what's next. J Sci Comput 2022;92(3):88.
[37] Ince A. Physics-informed deep neural network framework for prediction of fatigue crack growth in LPBF-manufactured metallic alloys. Int J Fatigue 2026:109522.
[38] Hijazi A, Al-Dahidi S, Altarazi S. Residual strength prediction of aluminum panels with multiple site damage using artificial neural networks. Materials 2020;13(22):5216.
[39] Al-Dahidi S, Gharaibeh MA, Alrbai M, Rinchi B, Hijazi A. An optimized hybrid finite element analyses-Artificial neural networks technique for estimating in-plane orthotropic mechanical properties of printed circuit boards. Results Eng 2024;23:102725.
[40] Young DG. Fatigue and fracture of elastomeric materials. Rubber World; (United States) 1991;204(1).
[41] Barbosa JF, Correia JA, Júnior RF, De Jesus AM. Fatigue life prediction of metallic materials considering mean stress effects by means of an artificial neural network. Int J Fatigue 2020;135:105527.
[42] Dubey SR, Singh SK, Chaudhuri BB. Activation functions in deep learning: a comprehensive survey and benchmark. Neurocomputing 2022;503:92–108.
[43] Rohman MN, Hidayat MIP, Purniawan A. Prediction of composite fatigue life under variable amplitude loading using artificial neural network trained by genetic algorithm. AIP Conference Proceedings. AIP Publishing LLC; 2018.
[44] Movahedi-Rad AV, Keller T. Load history effects in fiber–polymer composites: a CRNN-based hybrid deep learning approach for fatigue life prediction and structural health monitoring via infrared thermography. Comp Part A: Appl Sci Manuf 2025:109263.
[45] Long X, Guo Y, Su Y, Siow KS, Chen C. Unveiling the damage evolution of SAC305 during fatigue by entropy generation. Int J Mech Sci 2023;244:108087.
[46] Long X, Guo Y, Su Y, Siow KS, Chen C. A new unified creep-plasticity constitutive model coupled with damage for viscoplastic materials subjected to fatigue loading. Fatigue Fract Eng Mater Struct 2023;46(4):1413–25.

[47] Long X, Chong K, Su Y, Chang C, Zhao L. Meso-scale low-cycle fatigue damage of polycrystalline nickel-based alloy by crystal plasticity finite element method. Int J Fatigue 2023;175:107778.

[48] Iyela PM, Dong R, Jia F, Wan X, Chen C, Meng S, et al. Multiscale phase-field fracture modeling of sintered porous silver nanoparticles within a unified creep-plasticity framework. Int J Plast 2026:104729.

[49] He G, Zhao Y, Yan C. A data augmentation method for multiaxial fatigue life prediction based on physics-informed tabular generative adversarial network. Journal of Physics: Conference Series. IOP Publishing; 2024.